

Geostrophy Assessment and Momentum Balance of the Global Oceans in a Tide- and Eddy-Resolving Model

Xiaolong Yu¹ , Aurélien L. Ponte¹ , Noé Lahaye², Zoé Caspar-Cohen¹ , and Dimitris Menemenlis³ 

¹Ifremer, Université de Brest, CNRS, IRD, Laboratoire d'Océanographie Physique et Spatiale, IUEM, Brest, France, ²Inria & IRMAR, Campus Universitaire de Beaulieu, Rennes, France, ³Jet Propulsion Laboratory, California Institute of Technology, Pasadena, CA, USA

Key Points:

- We assess the accuracy of global geostrophy using instantaneous model snapshots in the context of the upcoming Surface Water Ocean Topography satellite
- Geostrophic balance explains over 80% of variance in the ocean's major current regions of high kinetic energy
- Everywhere else, geostrophic imbalance is dominated by fast variability (e.g., inertial and higher) and turbulent stress divergence

Supporting Information:

Supporting Information may be found in the online version of this article.

Correspondence to:

X. Yu,
xiaolong.yu@ifremer.fr

Citation:

Yu, X., Ponte, A. L., Lahaye, N., Caspar-Cohen, Z., & Menemenlis, D. (2021). Geostrophy assessment and momentum balance of the global oceans in a tide- and eddy-resolving model. *Journal of Geophysical Research: Oceans*, 126, e2021JC017422. <https://doi.org/10.1029/2021JC017422>

Received 30 MAR 2021

Accepted 9 SEP 2021

Abstract The future wide-swath satellite altimeters, such as the upcoming Surface Water Ocean Topography (SWOT) mission, will provide instantaneous 2D measurements of sea level down to the spatial scale of O(10 km) for the first time. However, the validity of the geostrophic assumption for estimating surface currents from these instantaneous maps is not known *a priori*. In this study, we quantify the accuracy of geostrophy for the estimation of surface currents from a knowledge of instantaneous sea level using the hourly snapshots from a tide- and eddy-resolving global numerical simulation. Geostrophic balance is found to be the leading-order balance in frontal regions characterized by large kinetic energy, such as the western boundary currents and the Antarctic Circumpolar Current. Everywhere else, geostrophic approximation ceases to be a useful predictor of ocean velocity, which may result in significant high-frequency contamination of geostrophically computed velocities by fast variability (e.g., inertial and higher). As expected, the validity of geostrophy is shown to improve at low frequencies (typically < 0.5 cpd). Global estimates of the horizontal momentum budget reveal that the tropical and mid-latitude regions where geostrophic balance fails are dominated by fast variability and turbulent stress divergence terms rather than higher-order geostrophic terms. These findings indicate that the estimation of velocity from geostrophy applied on SWOT instantaneous sea level maps may be challenging away from energetic areas.

Plain Language Summary The geostrophic balance, which is a balance between the Coriolis force and the pressure gradient force, is a fundamental assumption that enables the estimation of the surface ocean circulation from sea surface height maps. The validity of this approximation down to spatial scales of order 10 km is critical to next-generation satellite altimetry missions, such as the upcoming Surface Water and Ocean Topography (SWOT) mission with a scheduled launch date in late 2022. In this study, we assess the degree of geostrophic validity using the instantaneous output from a high-resolution global model including tidal forcing. Our results suggest that geostrophic balance is a satisfactory approximation in energetic regions, such as the western boundary currents and the Antarctic Circumpolar Current. This is not the case however for the bulk of subtropical and subpolar open-ocean regions, suggesting that directly assuming geostrophy in these regions may lead to biased time-varying estimates of velocity. High-frequency signals dominate the ageostrophic motions everywhere except in the Southern Ocean, where the low-frequency wind-driven currents take over. These results suggest that using geostrophy on the raw maps of sea level collected by SWOT will not lead to an accurate prediction of surface currents away from energetic areas.

1. Introduction

About 80% of the kinetic energy in the ocean is contained at the mesoscale, where rotational effects are dominant and flows are approximately balanced and geostrophic (Ferrari & Wunsch, 2009). Mesoscale eddies in the ocean include coherent vortical structures with characteristic spatial scales of tens to hundreds of kilometers and temporal scales of weeks to months. Our understanding of mesoscale eddies dynamics has significantly advanced over the last 30 yr owing to the availability of sea surface height (SSH) measurements that are routinely collected by satellite altimeters (Chelton et al., 2011; Morrow & Le Traon, 2012). The along-track SSH measurements from conventional nadir radar altimeters are typically merged and smoothed via objective analysis and optimal interpolation method to map SSH with uniform grid and global

coverage. In doing so, gridded SSH maps typically resolve signals with horizontal and temporal resolutions of $O(100\text{ km})$ and $O(1\text{ month})$; Ballarotta et al., 2019), and are widely used to infer the balanced flow field at the mesoscale and larger scales through the geostrophic approximation.

Submesoscale processes, characterized by smaller spatial scales of $O(1\text{--}10\text{ km})$ and shorter time scales (on the order of the local inertial period, Callies et al., 2020) than the mesoscale eddies, have come into focus more recently. Submesoscale motions are found to have an important contribution to vertical transport of buoyancy, nutrients, and other biogeochemical tracers (see, e.g., Lévy et al., 2018 for a review), and to transfer energy downscale from mesoscale eddies to small-scale turbulence (see, e.g., McWilliams, 2016 for a review). Dynamically, submesoscale processes are characterized by the Rossby number and bulk Richardson number on the order of unity (Thomas et al., 2008). They are posited to be in partial geostrophic balance because the equilibrium between Coriolis and horizontal pressure-gradient forces is altered by a more significant contribution from advection. Based on yearlong mooring observations, Yu, Naveira Garabato, et al. (2019) showed that geostrophy could explain approximately 56% of the variance of submesoscale subinertial flows at $\sim 2\text{-km}$ horizontal resolution. Submesoscale motions have been highlighted by a few very recent *in situ* observations to affect restratification of the upper ocean and to modulate the evolution of the mixed layer on climatic time scales (Du Plessis et al., 2019; Siegelman et al., 2020; Yu et al., 2021). Numerical studies further indicate that high-frequency submesoscale motions, including unbalanced inertia-gravity waves, may contribute to the vertical global heat transport equally as the subinertial balanced component (e.g., Su et al., 2020). Thus, investigating the dominance of balanced and unbalanced motions at the submesoscale and specifically, the degree of geostrophic validity, is a fundamental requirement to gauge the relative contributions of the two components, and to fully understand their respective roles in shaping the ocean's vertical transport and energy transfers (e.g., Schubert et al., 2020).

Investigations of geostrophic validity for instantaneous fields are motivated by the future wide-swath altimetry missions, such as the upcoming Surface Water and Ocean Topography (SWOT) altimeter mission (Morrow et al., 2019) and the Chinese “Guanlan” mission which is in the early designing stage (Chen et al., 2019). With the advent of wide-swath radar interferometry, the SWOT mission is expected to provide, for the first time, 2D sea level maps globally and at spatial scales down to 15–50 km depending on the local sea state (Callies & Wu, 2019; Wang et al., 2019). For SWOT, the estimation of surface velocity from the operational SSH maps may still be founded on the geostrophic approximation. However, the validity of geostrophy for estimating surface currents from instantaneous maps of sea level at such fine spatial scales is not known *a priori*. Besides the inherent measurement noise, critical challenges for the analysis SWOT data may also come from the long repeat cycle of SWOT orbit and the scale overlap between balanced motions and unbalanced inertia-gravity waves and their interactions (Klein et al., 2019; Lahaye et al., 2019; Ponte et al., 2017; Torres et al., 2018), which result in aliased variability associated with unbalanced motions in the SSH measurements. The inertia-gravity waves include internal waves and tides, near-inertial waves (NIWs) and internal wave continuum.

High-resolution ocean models that include astronomical tidal forcing provide a useful testbed to explore and unravel the issue of balance/unbalanced disentanglement in the SWOT mission. For instance, Qiu et al. (2018) indicated that the spatial transition length scale separating balanced geostrophic flows and unbalanced inertia-gravity waves on a global scale strongly depends on the energy level of local mesoscale eddy variability. Savage, Arbic, Richman, et al. (2017) provided global SSH variance associated with semidiurnal and diurnal tides and supertidal motions from a yearlong HYCOM output. The SSH signature of internal tides and internal wave continuum may result in contamination in the SSH-derived velocity estimates directly through geostrophy at the resolution of SWOT, as illustrated by a regional simulation in Chelton et al. (2019).

Low-frequency wind-driven currents represent another important component of the ageostrophic motions at the surface. The classical paradigm of the wind-driven current is founded on Ekman(1905) theory, which assumes a steady, linear, and vertically homogeneous ocean on a large spatial scale. The current arises from the balance between the Coriolis force and the vertical convergence of the turbulent stress due to the winds (Lagerloef et al., 1999). In this view, the vertical structure of the Ekman currents is a spiral rotating clockwise (anticlockwise) with depth in the Northern (Southern) Hemisphere, with a surface current directed at 45° to the right (left) of the wind in the Northern (Southern) Hemisphere. Recent studies have extended

this classical picture to time dependent configurations (e.g., Shrira & Almelah, 2020). Efforts have been put into approximating global wind-driven currents from reanalysis surface wind fields in order to isolate them from the SSH-derived surface velocity (e.g., Rio, 2003). Satellite missions that are still under development, such as Winds and Currents Mission (Rodriguez et al., 2018), the Surface Kinematic Monitoring (SKIM; Ardhuin et al., 2018) mission, and Ocean Surface Current multiscale Observation Mission (Du et al., 2021), aim at measuring simultaneously ocean surface winds and currents on a global scale using a Doppler scatterometer. The instantaneous current and wind measurements from these missions will allow a more direct estimation of geostrophic and Ekman currents globally.

In this study, we assess the accuracy of global geostrophy using instantaneous surface fields at hourly intervals from a tide- and eddy-resolving ocean simulation. Such model outputs are essential to assess the potential ability and limitation of geostrophy for estimating surface currents from 2D sea level maps that will be obtained from SWOT. We decompose the velocity field into two components: the geostrophic velocity computed from SSH derivatives in space directly from SSH rotated gradient and the other ageostrophic velocity defined as the difference between the total velocity and the geostrophic one. Note that this simple decomposition preserves all temporal scales of variability in the flow (including those that are not in geostrophic equilibrium). When directly applied to instantaneous SSH snapshots, this may result in the contamination of geostrophic velocity estimates by unbalanced fast variability. Thus, the reliability of geostrophic estimates will depend on the relative strength of low-frequency geostrophic turbulence versus high-frequency motions, on top of wind-driven currents. Fast variability refers to motions with inertial and higher frequencies in this work. The accuracy of the geostrophic approximation is assessed by comparing the kinetic energy levels of ageostrophic and total horizontal velocities geographically and spectrally, and we then explore the governed momentum balance underpinning the regions where geostrophy fails. The article is organized as follows. Section 2 introduces the simulation, the momentum balance framework, and methods of velocity decomposition and spectral analysis. Diagnostics about geostrophic accuracy are described in Section 3 along with a more detailed investigation of surface momentum equilibriums. Discussions and conclusions are offered in Sections 4 and 5, respectively.

2. Materials and Methods

2.1. LLC4320 Simulation

The output from a state-of-the-art global numerical simulation, namely LLC4320 (Su et al., 2018), is employed to assess the validity of geostrophic approximation and horizontal momentum balances at the surface layer of the global oceans. The LLC4320 simulation was performed using the MITgcm (Marshall et al., 1997) on a global latitude-longitude-cap (LLC) grid (Forget et al., 2015) for a period of 14 months between 10 September 2011 and 2015 November 2012. The model has a horizontal grid spacing of $1/48^\circ$ (approximately 2.3 km at the equator and 0.75 km in the Southern Ocean), and thereby resolves mesoscale eddies and part of the internal wave field and permits submesoscale variability. The model time step was 25 s, and model variables were stored at hourly intervals. The model was forced at the surface by six-hourly surface flux fields (including 10-m wind velocity, 2-m air temperature and humidity, downwelling long- and short-wave radiation, and atmospheric pressure load) from the ECMWF operational reanalysis, and included the full luni-solar tidal constituents that are applied as additional atmospheric pressure forcing. The LLC4320 uses a flux-limited monotonicity-preserving (seventh order) advection scheme, and the modified Leith scheme of Fox-Kemper and Menemenlis (2008) for horizontal viscosity. The K -profile parameterization (Large et al., 1994) is used for vertical viscosity and diffusivity. In this study, we use a yearlong record of the instantaneous surface fields at every hour, starting on 15 November 2011.

Physical processes captured by the simulation are illustrated with an SSH snapshot on November 24, 2011 (Figure 1). It includes a large-scale circulation with embedded mesoscale meanders and eddies (e.g., in the Southern Ocean) and internal tides (e.g., east of the Luzon Strait). Coastal regions, defined here as the areas with seafloor depths shallower than 500 m, are mainly influenced by barotropic tides. Coastal regions show distinct features (e.g., periodic amplitudes of SSH and velocity; see Movie S1) to open ocean regions. Furthermore, polar regions (mostly located in the areas with latitudes higher than 60°) are covered by sea ice seasonally or all year round. In the following analysis, we exclude both coastal and ice-covered regions on the basis that they deserve dedicated studies.

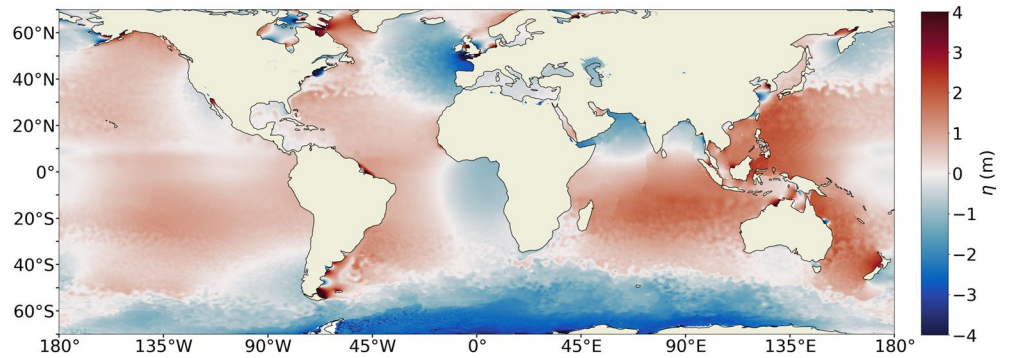


Figure 1. Snapshot of the sea surface height at 08:00 on 24 November 2011 from the LLC4320 simulation.

2.2. Vector-Invariant Momentum Equation

The vector-invariant form of the momentum equation is used to analyze the momentum balances at the surface layer in the LLC4320 simulation. An advantage of the vector-invariant momentum equation is its generality, as it is invariant under coordinate transformations:

$$\frac{\partial \vec{u}}{\partial t} + \underbrace{\vec{k}\zeta \times \vec{u} + \nabla \left(\frac{1}{2} \vec{u}^2 \right)}_{\vec{u} \cdot \nabla \vec{u}} + \underbrace{f \times \vec{u} + g \nabla \eta}_{f \times \vec{u}_a} = \vec{R}, \quad (1)$$

where $\vec{u} = (u, v)$ is the 2-day velocity vector, t is the time, \vec{k} is the vertical unit vector, ζ is the vertical component of relative vorticity, ∇ is the spatial gradient operator, $f = 2\Omega \sin \phi$ is the Coriolis parameter (with Ω as Earth's angular velocity and ϕ as latitude), g is the gravitational acceleration, η is the SSH, and \vec{R} is a residual term. The terms in the vector-invariant momentum equation are estimated using the hourly instantaneous output (i.e., off-line). The year-long time series of surface velocity and SSH fields are used to diagnostically estimate the terms of Equation 1.

The time acceleration term, $\frac{\partial \vec{u}}{\partial t}$, is calculated as a first-order derivative by a forward difference in time. Assuming small vertical advection (i.e., $w \frac{\partial \vec{u}}{\partial z}$ where w is the vertical velocity), the advection term, $\vec{u} \cdot \nabla \vec{u}$, is estimated as the sum of the nonlinear Coriolis term ($\vec{k}\zeta \times \vec{u}$) and the kinetic energy divergence term ($\nabla \left(\frac{1}{2} \vec{u}^2 \right)$). The sum of the linear Coriolis term ($f \times \vec{u}$) and the horizontal pressure gradient term ($g \nabla \eta$) yields $f \times \vec{u}_a$. This term represents the Coriolis force acting on the ageostrophic flow, and is referred to as the ageostrophic Coriolis term in this study. The residual term, \vec{R} , is estimated as the sum of the terms on the left-hand side of Equation 1. Note that \vec{R} includes the momentum contributions from turbulent stress divergence associated with atmospheric forcing and horizontal dissipation, vertical advection, sub-grid processes, and all possible errors involved in the estimation process (e.g., discretization error associated with the hourly output sampling). Another source of error in the momentum budget stems from the difference between the vector-invariant momentum equation used in the analysis and the Eulerian flux-form momentum equation used in the model. This error will be a fraction of the true advective term, and is likely negligible because the advection term is not a significant term in the momentum budget (Section 3.3).

2.3. Geostrophic/Ageostrophic Decomposition

The geostrophic balance typically holds for ocean motions characterized by small Rossby number ($Ro \ll 1$) and low frequency (lower than the local inertial frequency; Vallis, 2006). If these conditions are met, a balance exists between Coriolis and pressure gradient forces,

$$f \times \vec{u}_g = -g \nabla \eta, \quad (2)$$

where $\vec{u}_g = (u_g, v_g)$ is the geostrophic velocity vector.

With the primary goal of evaluating the reliability of velocity estimates via geostrophy in the context of SWOT, the time-varying horizontal velocity is computed geostrophically from the instantaneous SSH field from the model output,

$$u_g = -\frac{g}{f} \frac{\partial \eta}{\partial y}, v_g = \frac{g}{f} \frac{\partial \eta}{\partial x}. \quad (3)$$

As illustrated in Chelton et al. (2019), the velocity diagnostics computed geostrophically from tide-resolving instantaneous SSH snapshots should be regarded differently from the geostrophic component of velocity that is valid only for small Rossby number and low frequency. Following their work, we refer to these estimates of geostrophic velocity (u_g, v_g) as geostrophically computed velocity. The potential limitations of velocity estimates from an instantaneous tide-resolving SSH map according to the geostrophic balance will be discussed in Section 4. The ageostrophic velocity (u_a, v_a) is defined as the difference between the total and geostrophically computed velocity,

$$u_a = u - u_g, v_a = v - v_g. \quad (4)$$

2.4. Frequency Rotary Spectrum

The yearlong time series of the surface horizontal velocity (u, v), geostrophically computed velocity (u_g, v_g) and ageostrophic velocity (u_a, v_a) are respectively used to estimate their rotary spectra at model grid points. We first divide velocity time series into segments of 60 days overlapping by 50% and linearly detrend over each segment, and then compute the 1D discrete Fourier transform of complex-valued fields (e.g., $u + iv$) multiplied by a Hanning window. The spectra are formed by multiplying the Fourier coefficients by their complex conjugates, and the spectra are averaged over segments. Following Elipot et al. (2010), the cyclonic Coriolis frequency is defined as f and the anticyclonic inertial frequency as $-f$. We also integrate rotary frequency spectral densities over five frequency bands to compute kinetic energy components of interest, including high-frequency (>0.5 cpd, absolute values here and hereinafter), near-inertial ($0.9-1.1f$), semi-diurnal ($1.9-2.1$ cpd), diurnal ($0.9-1.1$ cpd), and supertidal (>2.1 cpd). Our results are insensitive to the choice of the band limits (Yu, Ponte, et al., 2019). The kinetic energy components estimated from windowed spectra are then multiplied by a factor of 8/3 to compensate for the Hanning windowing operation (Emery & Thomson, 2001). Total kinetic energy is estimated from temporal averages of instantaneous fields, and low-frequency kinetic energy is computed as a total kinetic energy minus high-frequency kinetic energy.

3. Results

3.1. Comparison of Surface Kinetic Energy Estimates

The global snapshots of the zonal component of total velocity, geostrophically computed velocity and ageostrophic velocity are shown in Figure 2. At mid-latitudes ($30^\circ-60^\circ$ N and S), the zonal velocity, u , compares visually well with the geostrophically computed velocity, u_g . This is especially true for the signature of energetic features, including the Gulf Stream, the Kuroshio Extension, the Brazil Current, the Agulhas Current, and the Eastern Australian Current. The ageostrophic velocity, u_a , exhibits a spatial structure of $O(1,000$ km) superimposed with wave-like signals of $O(100$ km). A somewhat different picture is seen in the tropical and subtropical regions ($30^\circ\text{S}-30^\circ\text{N}$), where u reflects an alternating zonally elongated current system with typical amplitudes of the order to 1 m s^{-1} and vigorous internal wave features such as in the southeast of the Luzon Strait. Both u_g and u_a exhibit, on the other hand, remarkably fine-scale wave-like structures associated with amplitudes greatly exceeding that of the full velocity field. These unrealistically large u_g and u_a mirror each other, and arise from the small-scale high-frequency variability in the SSH field (Figure S1) combined with reduced Coriolis parameter f near the equator. This highlights challenges for the estimation of surface velocity from future altimetric high-resolution SSH maps through geostrophic approximation at low latitudes. We exclude equatorial latitudes ($10^\circ\text{S}-10^\circ\text{N}$) in the following geostrophy assessment, but will explore the governing dynamics in the framework of momentum balance for the equatorial ocean in Section 3.3. The global distribution of the year-mean surface kinetic energy, KE , indicates that the ocean's kinetic energy is dominated by mesoscale-to-large-scale circulations in the regions of western boundary currents, the Antarctic Circumpolar Current (ACC) and the equatorial ocean (Figure 3). The magnitudes of kinetic energy in these energetic regions are on the order of $O(1 \text{ m}^2 \text{ s}^{-2})$, exceeding typical

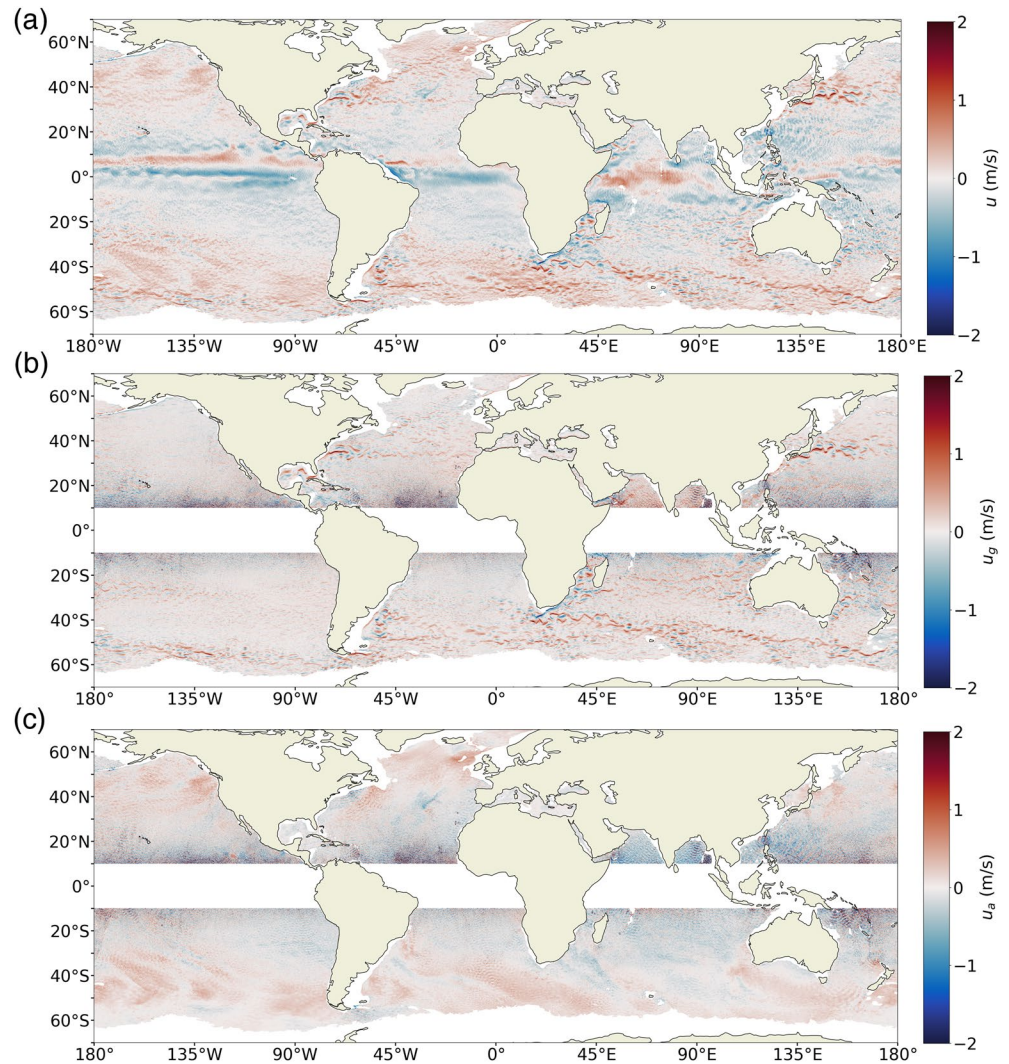


Figure 2. Snapshot of (a) the surface zonal velocity, (b) the zonal component of geostrophically computed velocity, and (c) the zonal component of ageostrophic velocity at 08:00 on 24 November 2011 from the LLC4320 simulation. The coastal and ice-covered regions are excluded.

values in the vast areas of other open-ocean regions (e.g., the eastern boundary current region of each ocean basin) by at least one order of magnitude. These modeled features of kinetic energy are broadly consistent with global drifter observations (Lumpkin & Johnson, 2013). In the energetic regions, patterns of kinetic energy resemble that associated with geostrophically computed velocity, KE_g , indicating that the geostrophic component could explain much of the variance in these regions. By contrast, in other open-ocean regions (such as the mid-latitude South Pacific and low latitudes), the geostrophic and ageostrophic kinetic energies, KE_g and KE_a , are both orders of magnitude larger than the total kinetic energy, which indicates surface velocity field cannot reliably be estimated using the geostrophic approximation. As for snapshots, both KE_a and KE_g diverge in the equatorial oceans due to the vanishing Coriolis parameter. Lastly, there is no clear correspondence between KE_a and KE patterns, suggesting that higher-order geostrophic terms (e.g., cyclo-geostrophic balance; Penven et al., 2014) may contribute only modestly to the ageostrophic circulation at a global scale. The frequency rotary spectra of surface total velocity (\tilde{E}), geostrophically computed velocity (\tilde{E}_g) and ageostrophic velocity (\tilde{E}_a) as a function of latitude and frequency are shown in Figure 4. The velocity spectra are characterized by high-energy peaks at low frequencies (<0.5 cpd), diurnal, semidiurnal, and latitude-varying inertial frequencies. At low frequencies, the high-energy peaks of the surface total velocity field are reflected in geostrophic rotary spectra across all latitudes, whereas the ageostrophic rotary spectra

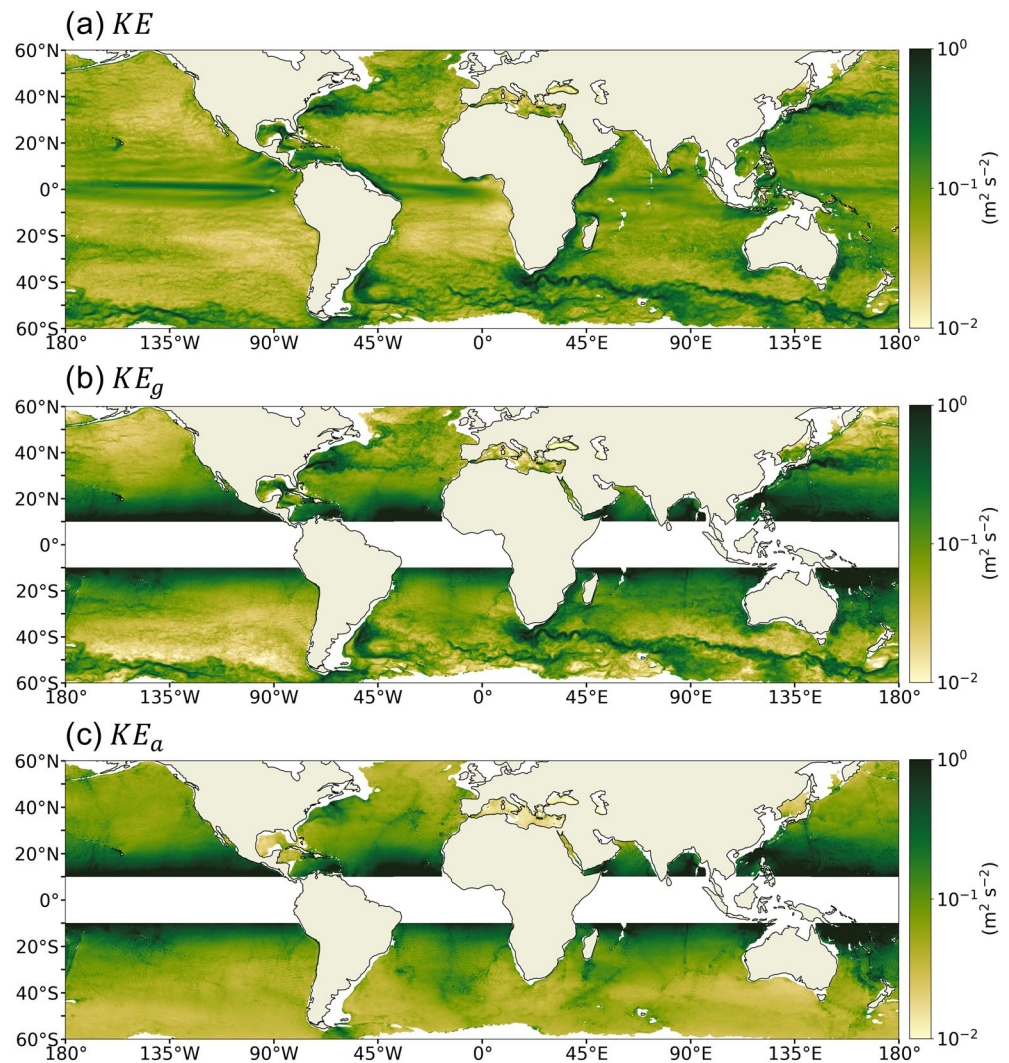


Figure 3. Global distributions of annually averaged (a) total, (b) geostrophically computed and (c) ageostrophic kinetic energies at the ocean surface from the LLC4320 simulation.

peak more moderately. This is consistent with the expectation that low-frequency motions are dominantly in geostrophic balance (Vallis, 2006). Indeed, the low-frequency component of the geostrophically computed kinetic energy, $KE_{g,low}$, is two to five times larger than that of the ageostrophic kinetic energy, $KE_{a,low}$, away from the equatorial band. This highlights that the low-frequency total kinetic energy (which accounts for approximately 80% of the total kinetic energy globally), KE_{low} , is mainly composed of slow geostrophic motions (Figure 5a).

At high frequencies (>0.5 cpd), spectra estimated from geostrophically computed velocity and ageostrophic velocity exceed the total velocity spectra, especially at diurnal, semidiurnal and higher tidal harmonic frequencies, indicating a failure of geostrophy at these frequencies. The energy peaks at the latitude-varying inertial frequencies are purely ageostrophic, due to the minor role played by pressure gradients for NIWs. The failure of geostrophy for tidal and near-inertial motions is expected, because the inertia-gravity waves intrinsically relate to sea level according to polarization relations, which are a different dynamical link between pressure gradient and horizontal velocity than the geostrophic relation (Gill, 1982). This intrinsic nature of internal waves (i.e., following the polarization relations rather than the geostrophic relation) results in the overly large tidal peaks in geostrophically computed and ageostrophic spectra. Under linear dynamics, pressure gradient spectra approximately correspond to velocity spectra times a factor of ω^2/f^2 (where ω is frequency) for super-inertial frequencies (Callies et al., 2020).

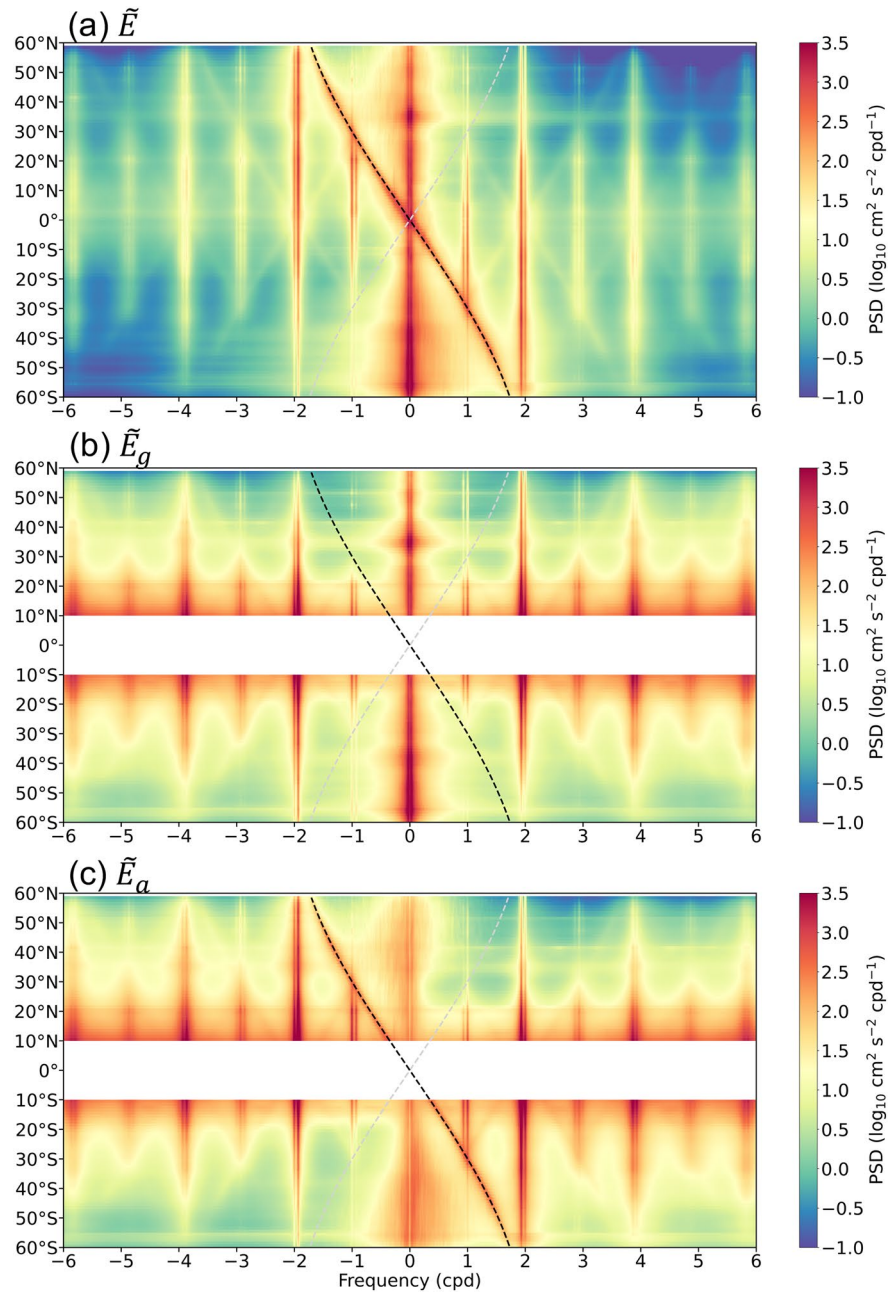


Figure 4. Zonally averaged rotary frequency spectra in 1° latitude bins from (a) total, (b) geostrophically computed, and (c) ageostrophic velocity fields at the surface layer of the LLC4320 simulation, with positive (negative) frequencies corresponding to counterclockwise (clockwise) rotating motions, which are cyclonic (anticyclonic) in the Northern Hemisphere. The cyclonic Coriolis frequency ($f/2\pi$ cpd) is indicated by the gray dashed line and the anticyclonic inertial frequency ($-f/2\pi$ cpd) is indicated by the black dashed line.

Additional understanding of the contamination of geostrophically computed velocity estimates by unbalanced motions may be gained by investigating the resulting ageostrophic kinetic energy, KE_a , which can be decomposed into components of different frequency bands using the spectra (Figure 5b). The low-frequency component, $KE_{a,low}$, tends to contribute increasingly to KE_a from low to high latitudes, and accounts for over 60% of KE_a in the Southern Ocean. As expected from the polarization relations, supertidal motions (typically $\omega \gg f$) are the dominant contributor to KE_a in the internal wave field, especially in tropical latitudes (also see Figure S2). Semidiurnal tides are the second largest component with the ratio $KE_{a,semi}/KE_a$

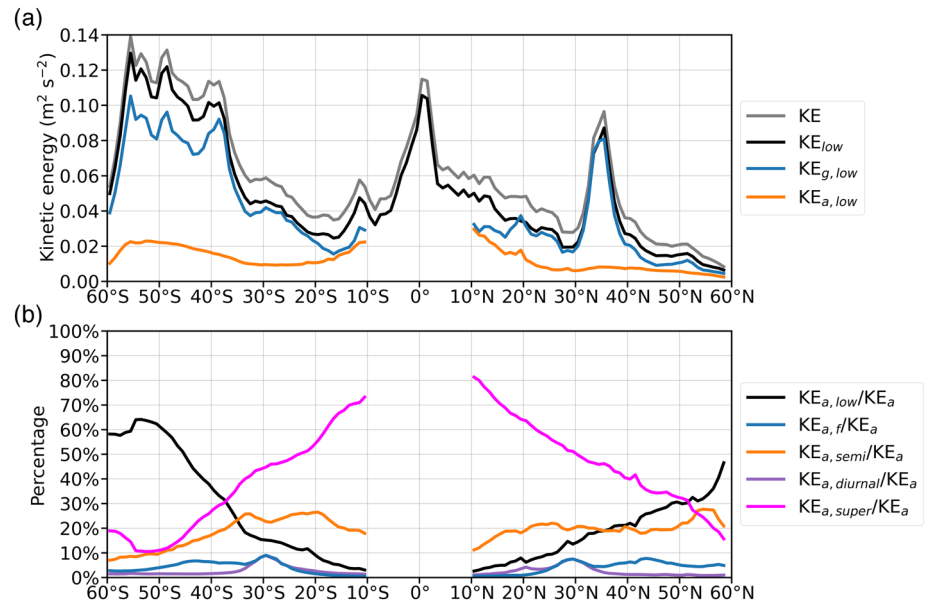


Figure 5. (a) Comparison of the zonally averaged total kinetic energy (gray), low-frequency component of total (black), geostrophically computed (blue), and ageostrophic (orange) kinetic energies in 1° latitude bins. (b) Percentage of low-frequency (black), near-inertial (blue), semidiurnal (orange), diurnal (purple) and supertidal (magenta) kinetic energies to the ageostrophic kinetic energy in 1° latitude bins.

between 10% and 30% across latitudes. In contrast, NIWs and diurnal tides make only a modest contribution to the ageostrophic kinetic energy, up to 10%.

3.2. Geostrophy Assessment

The ratio of ageostrophic kinetic energy to total kinetic energy, KE_a/KE , is used as a quantification of geostrophic validity (Figure 6a). A threshold of ratio 0.2 is chosen arbitrarily here. The global map of KE_a/KE illustrates the dominant geostrophic character of the velocity field in the regions of energetic kinetic energy, primarily in the western boundary currents and the ACC in the subpolar region. The ratio KE_a/KE is commonly smaller than 0.2 there, which means that geostrophic motions account for more than 80% of the total kinetic energy (i.e., geostrophy explains more than 80% of the variance). On the other hand, the estimated ageostrophic motions exhibit unreliable energy levels that are comparable or larger than the total kinetic energy in most of the open-ocean regions, including the Canary Current, Benguela Current, the California Current, and Peru Current. The large ratio of ageostrophic velocity to total velocity (e.g., $KE_a/KE > 1$) indicates the geostrophic decomposition is not meaningful over most of the ocean and geostrophic velocities are not accurate estimators of the circulation.

For low-frequency motions, the ratio $KE_{a, low}/KE_{low}$ is significantly reduced globally away from the equatorial ocean (Figure 6b). In the zonal average, the ratio KE_a/KE reaches its minimum of approximately 30% in the Southern Ocean, and down to below 50% at latitudes of the Kuroshio and the Gulf Stream (30°–40°N; Figure 6d). Zonally-averaged $KE_{a, low}/KE_{low}$ is always lower than that of KE_a/KE , with a range of 10%–60% at extratropical latitudes. Particularly, the ratio $KE_{a, low}/KE_{low}$ decreases to 20% in the Southern Ocean and to 10% in the 30°–40°N band.

In order to gain deeper insight into the temporal scale of the validity of geostrophic balance, the ratio of the rotary frequency spectra of ageostrophic velocity to total velocity (\bar{E}_a/\bar{E}) is computed (Figure 7). Across all latitudes, super-inertial (i.e., frequencies exceeding f) motions are dominated by ageostrophic dynamics. There is an obvious asymmetry between cyclonic and anticyclonic motions within the subinertial band (i.e., frequencies lower than f), where cyclonic motions appear to be more geostrophic at higher frequencies. For instance, the frequency scale for the validity of geostrophy under a 0.2 ratio threshold is approximately 0.15 cpd (i.e., 6.7 days) for cyclonic motions and 0.05 cpd (i.e., 20 days) for anticyclonic motions at latitudes

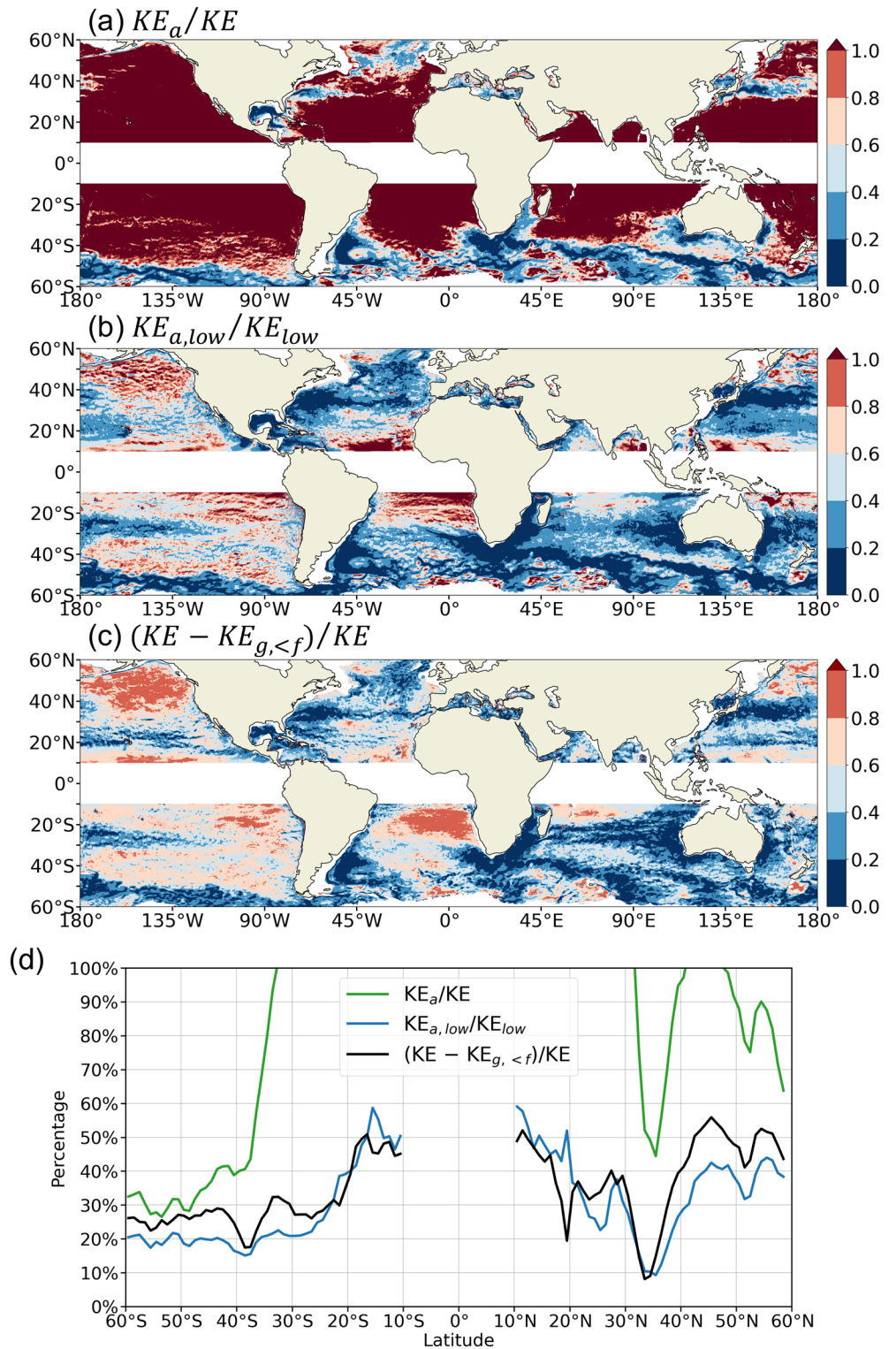


Figure 6. (a) Global map of the ratio between ageostrophic kinetic energy KE_a and total kinetic energy KE . (b) Global map of the ratio between low-frequency ageostrophic kinetic energy $KE_{a,low}$ and low-frequency total kinetic energy KE_{low} . (c) Global map of the ratio between $KE - KE_{g,<f}$ and KE . (d) Zonally averaged KE_a/KE (green), $KE_{a,low}/KE_{low}$ (blue), and $(KE - KE_{g,<f})/KE$ (black) in 1° latitude bins.

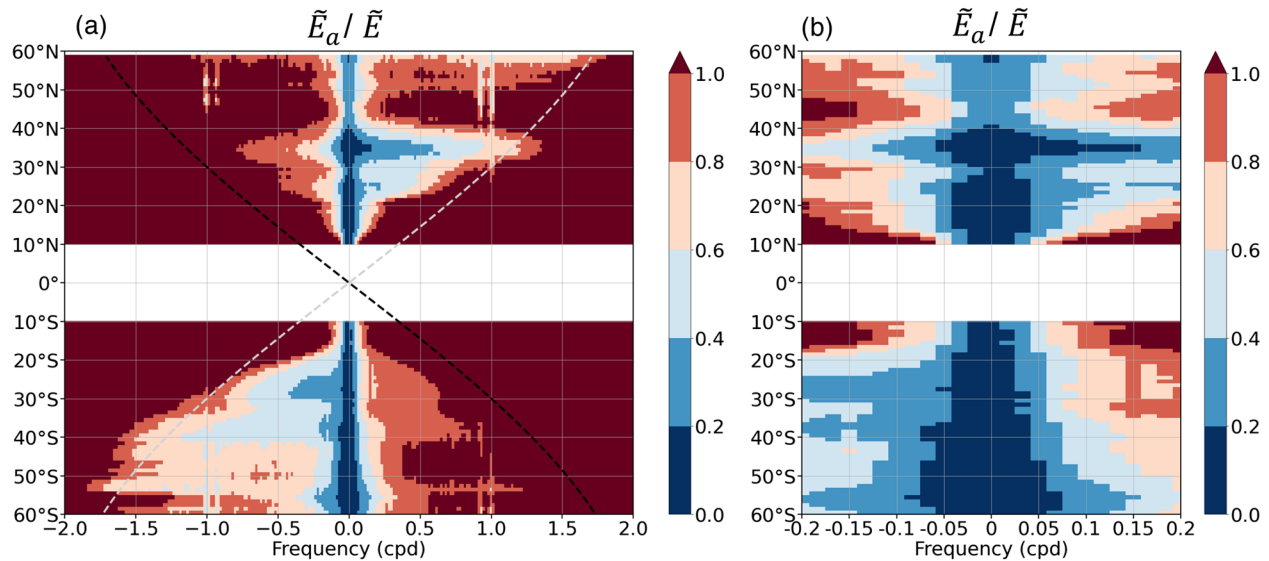


Figure 7. (a) The ratio of zonally averaged rotary frequency spectra from the ageostrophic velocity field and the total velocity field, \tilde{E}_a/\tilde{E} , at the surface layer of the LLC4320 simulation in 1° latitude bins. The cyclonic Coriolis frequency ($f/2\pi$ cpd) is indicated by the gray dashed line and the anticyclonic inertial frequency ($-f/2\pi$ cpd) is indicated by the black dashed line. (b) Same as (a) but zoomed in over the frequency range between -0.2 and 0.2 cpd.

of the Kuroshio and the Gulf Stream (30° – 40° N). This asymmetry is possibly due to the strongly polarized signature of NIWs extending down to lower frequencies under the influence of mesoscale eddies. The stronger influence of NIWs combined with their purely ageostrophic character would result in anticyclonic motions less geostrophic than cyclonic ones. Overall, the surface flows at frequencies less than approximately 0.05 cpd (i.e., periods longer than 20 days) follow the geostrophy balance ($\tilde{E}_a/\tilde{E} \sim 0.2$) to a first order, except in the quiescent subpolar region of the Northern Hemisphere and in the equatorial region where geostrophy does not hold due to the vanishing Coriolis parameter. This illustrates the expected result that the majority of large-scale gyres in the global oceans are in geostrophic balance at low frequencies.

3.3. Momentum Balance

In order to identify more specifically sources of ageostrophic variability, we compute the annual root mean square (denoted as $\langle \cdot \rangle_{rms}$) of each term in Equation 1.

The global distributions of the root-mean-square values of the linear Coriolis and pressure gradient forces are displayed in Figure 8. Consistent with the regions of small KE_a/KE ratios (Figure 6a), both two terms show enhanced values in energetic regions (e.g., the Southern Ocean and western boundary current system and extensions). One significant difference between the two terms is that the pressure gradient term also exhibits intense beam-like structures in the tropical region, whereas the linear Coriolis term is largely muted due to vanishing f . These beams emanate from known energetic internal tide generation sites (e.g., Amazon plateau and West of Luzon strait; Beardsley et al., 1995; Ray & Zaron, 2016; Zhao, 2014), which suggests that they are the signature of propagating internal tides. The signature of these beams is also present on the root mean square of the acceleration term, albeit with a weaker amplitude, and on the residual term (Figure 9). Internal tides of large amplitudes may be associated with significant advection of momentum and/or may evolve rapidly compared to the model output frequency, which would both explain their signature on the residual. The advection term is only profound in regions of large kinetic energy, and shows qualitatively similar patterns to the linear Coriolis term but with a magnitude a factor of 2–5 smaller.

The zonally averaged root-mean-square values of the horizontal pressure gradient term are comparable in magnitude with those of the linear Coriolis term at mid-latitudes (Figure 10a). The amplitude of ageostrophic Coriolis term ($\langle f \times \tilde{u}_a \rangle_{rms}$) closely follows the pressure gradient one between 0° – 30° N and S, where the value of the linear Coriolis term decreases with decreasing latitudes. The root mean square of the momentum balance residual covaries with $\langle f \times \tilde{u}_a \rangle_{rms}$, albeit with a smaller amplitude (Figure 10b). The time

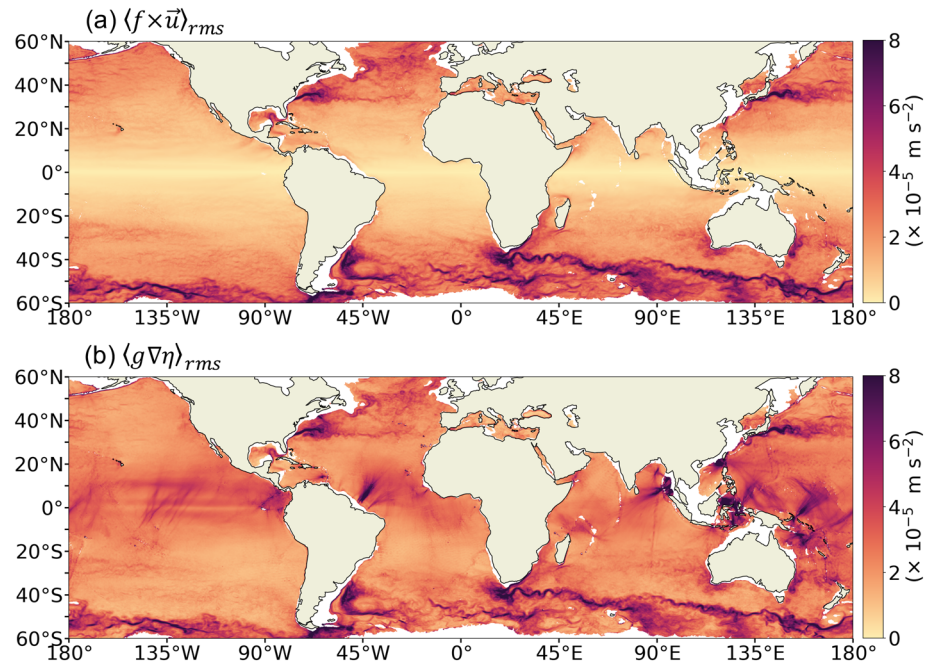


Figure 8. Global distributions of the root-mean-square values of (a) the linear Coriolis term $\langle f \times \bar{u} \rangle_{rms}$ and (b) the pressure gradient term $\langle g \nabla \eta \rangle_{rms}$.

acceleration term also broadly follows the latitudinal structure of $\langle f \times \bar{u}_a \rangle_{rms}$, and tend to have an increasing contribution momentum at low latitudes. Comparison of the ratio of each term to $\langle f \times \bar{u}_a \rangle_{rms}$ in Figure 11 shows that the acceleration and residual have comparable amplitudes with $\langle f \times \bar{u}_a \rangle_{rms}$ in the tropical region, which suggest a necessary cancellation between both terms. We have argued that the residual may be explained at the equator by the signature of large internal tides. At mid-latitudes, the residual term dominates $\langle f \times \bar{u}_a \rangle_{rms}$, and we speculate this residual is dominated by vertical stress divergence associated with winds. This is suggested by the lower frequency content of the residual (Figure S3) and its geographical distribution (Figure 11c). Finally, the advection term only makes up a moderate fraction of $\langle f \times \bar{u}_a \rangle_{rms}$ over the global oceans, approximately 10% in the subtropical regions and up to 30% in the subpolar regions.

4. Discussion

In the previous section, the global validity of geostrophy using the instantaneous model fields was shown to be latitude- and frequency-dependent. We now discuss possible biases and limitations from our model study. The LLC4320 simulation exhibits variance four times higher in the semidiurnal band and three times lower in the inertial band compared with surface drifter data (Yu, Ponte, et al., 2019). The tidal motions in LLC4320 are also found to be larger compared to those in other high-resolution global simulations, such as the HYbrid Coordinate Ocean Model with a horizontal grid spacing of $1/25^\circ$ (Luecke et al., 2020). The overly energetic semidiurnal tides, which are ubiquitous over the global oceans, would overestimate ageostrophic kinetic energy levels and thus lead to an underestimate of the degree of geostrophy validity. On the other hand, the deficit of the modeled near-inertial kinetic energy (which is purely ageostrophic) would lead to an optimistic geostrophy assessment.

The accuracy of geostrophic predictions of instantaneous sea level maps will be quantitatively improved from a simulation with more realistic levels of the unbalanced inertia-gravity waves. Numerically, an increase of spatial and temporal resolutions of wind forcing is a key step to improving the near-inertial kinetic energy levels (Flexas et al., 2019; Rimac et al., 2013). The magnitude of internal tides is found to be sensitive to model damping parameterizations, such as a parameterized topographic internal wave drag which is not included in MITgcm (Arbic et al., 2018). For LLC4320, there is also some speculation that the overly large semidiurnal tides may be partially caused by mistakes in the implementation of the ocean self-attraction

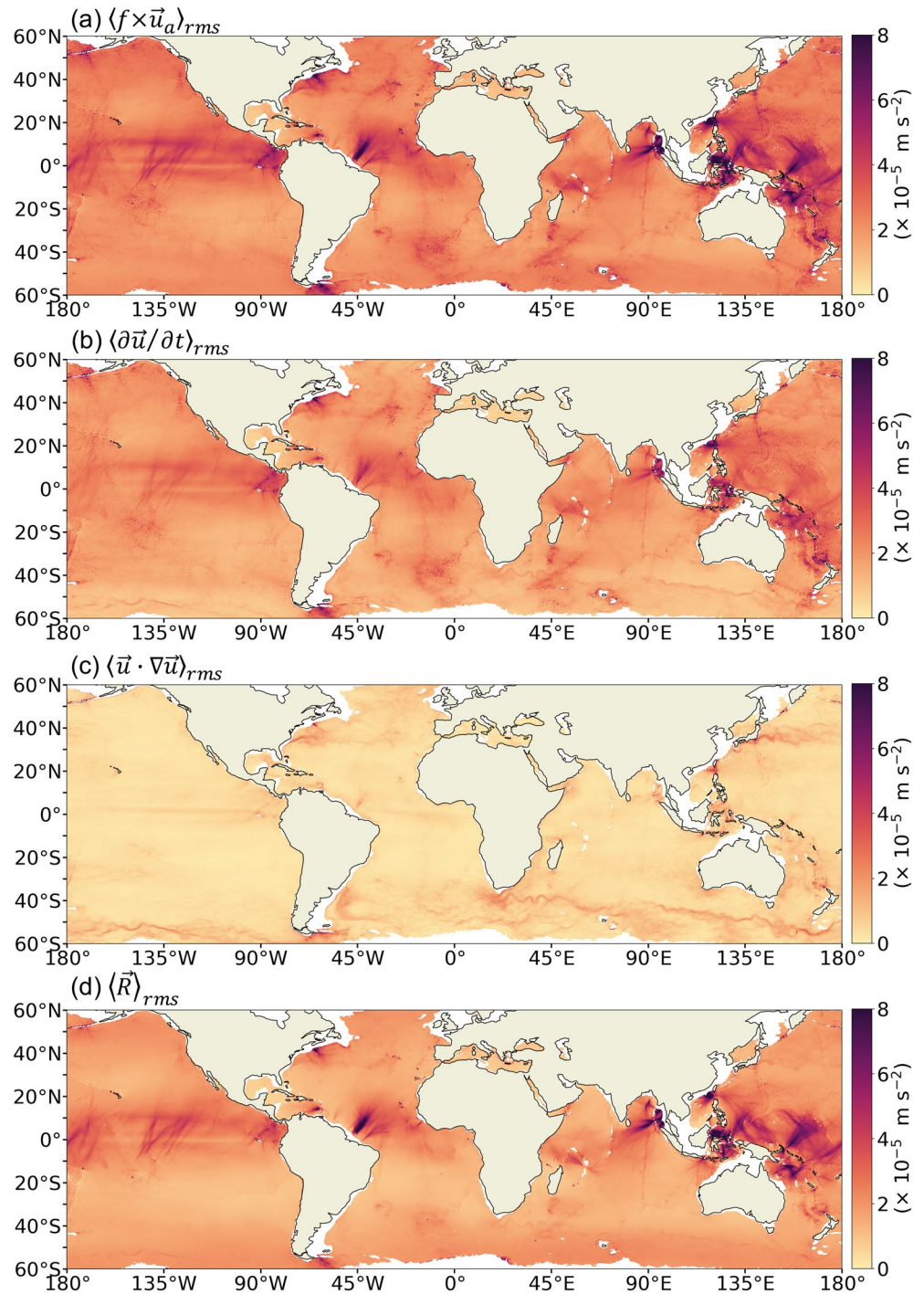


Figure 9. Global distributions of the root-mean-square values of (a) the ageostrophic Coriolis term $\langle f \times \bar{u}_a \rangle_{rms}$, (b) the time acceleration term $\langle \partial \bar{u} / \partial t \rangle_{rms}$, (c) the nonlinear advection term $\langle \bar{u} \cdot \nabla \bar{u} \rangle_{rms}$, and (d) the residual term $\langle \bar{R} \rangle_{rms}$.

and loading. Furthermore, recent modeling studies suggested that increasing the model horizontal resolution improves the comparison of modeled internal wave continuum with observations (Müller et al., 2015; Nelson et al., 2020; Savage, Arbic, Alford, et al., 2017).

A more dynamically relevant assessment of geostrophy may be obtained if only low-frequency contributions are accounted for geostrophic motions. To do so, the geostrophic kinetic energy associated with low-frequency motions is estimated as the subinertial band of KE_g , denoted as $KE_{g,<f}$. The ageostrophic kinetic

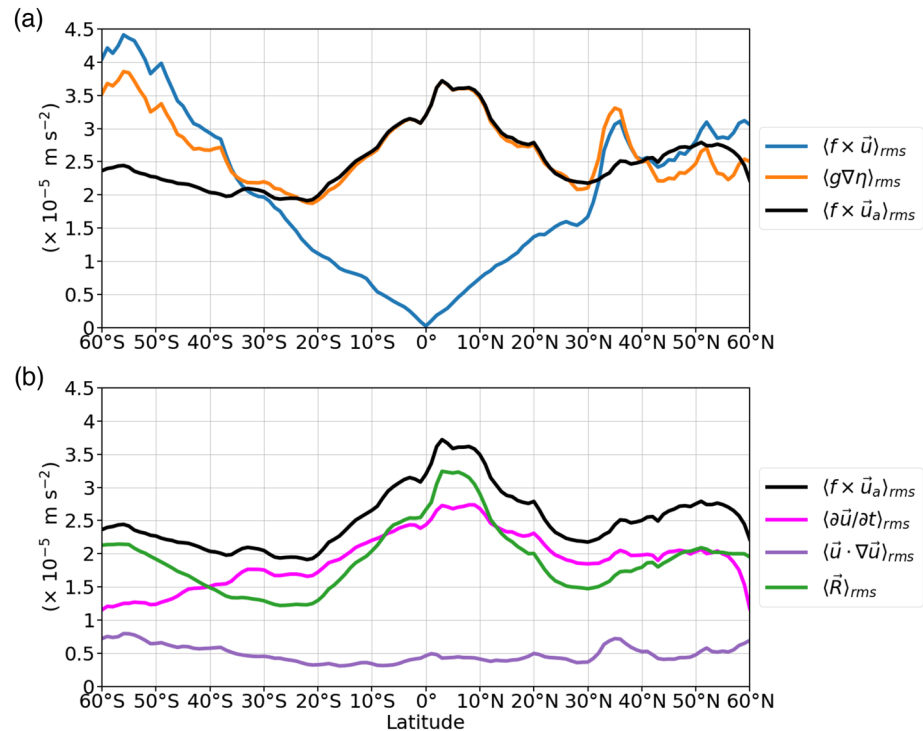


Figure 10. (a) Zonally averaged root-mean-square values of the linear Coriolis term ($\langle f \times \bar{u} \rangle_{rms}$, blue), the pressure gradient term ($\langle g \nabla \eta \rangle_{rms}$, orange), and the ageostrophic Coriolis term ($\langle f \times \bar{u}_a \rangle_{rms}$, black). (b) Same as (a) but for the time acceleration term ($\langle \partial \bar{u} / \partial t \rangle_{rms}$, magenta), the advection term ($\langle \bar{u} \cdot \nabla \bar{u} \rangle_{rms}$, purple), and the residual term ($\langle \bar{R} \rangle_{rms}$, green). The ageostrophic Coriolis term ($\langle f \times \bar{u}_a \rangle_{rms}$, black) is also shown as a reference.

energy is thus calculated as $KE - KE_{g,<f}$. We found that the ratio $(KE - KE_{g,<f})/KE$ and $KE_{a,low}/KE_{low}$ exhibit broadly similar spatial patterns (cf. Figures 6b and 6c) and zonal averages (Figure 6d). This suggests that subinertial geostrophic motions dominate energy levels in regions of large kinetic energy, and are comparable in magnitude to ageostrophic motions in most of the mid-gyre areas. Note that LLC4320 is one of the most realistic high-resolution global ocean models that at best permit submesoscale flows, and thus subinertial submesoscale flows are accounted as geostrophic motions in this analysis (Figure 6c). A follow-up study on the effects of submesoscale flows on the validity of geostrophic approximation would require spatial filtering of the surface fields with several different cutoff wavelengths. This point is also discussed in Section 5 in the SWOT context.

Practically speaking, the contamination of NIWs will be a greater challenge for near-nadir Doppler radar missions such as SKIM than for satellite altimetry missions such as SWOT (see Figure S1 as an illustration that NIWs have almost no signature on the SSH field). Another challenge is that instrumental noise levels inevitably prevent the analysis of raw sea level maps provided by SWOT and an averaging may be required (Chelton et al., 2019). A temporal average could also smooth both instrumental noise and the high-frequency variability that affects the accuracy of geostrophic currents for the estimation of surface currents. Time-averaged fields may be constructed either from repeated measurement swaths or from combing multiple satellite measurements. Moreover, one may speculate on the potential of having simultaneous maps of sea level (from SWOT) and surface currents (from SKIM) to improve our understanding of high-frequency motions (e.g., one could directly compute observed ageostrophic currents via the combination of the two).

Motivated by the moderate amplitude (of order 10 mbar) and large spatial scales (of order 1,000 km) of atmospheric surface pressure fluctuations and hence their small contribution to surface pressure gradients (Fu & Pihos, 1994; Wunsch & Stammer, 1997), this study ignored the contribution of the atmospheric pressure load in the calculation of ocean pressure. Sea level responses to atmospheric fluctuations of the inverted barometer type contribute here to geostrophic currents estimates, while they should have not. We believe this is a small inaccuracy that future studies can quantify and remedy provided access to the forcing

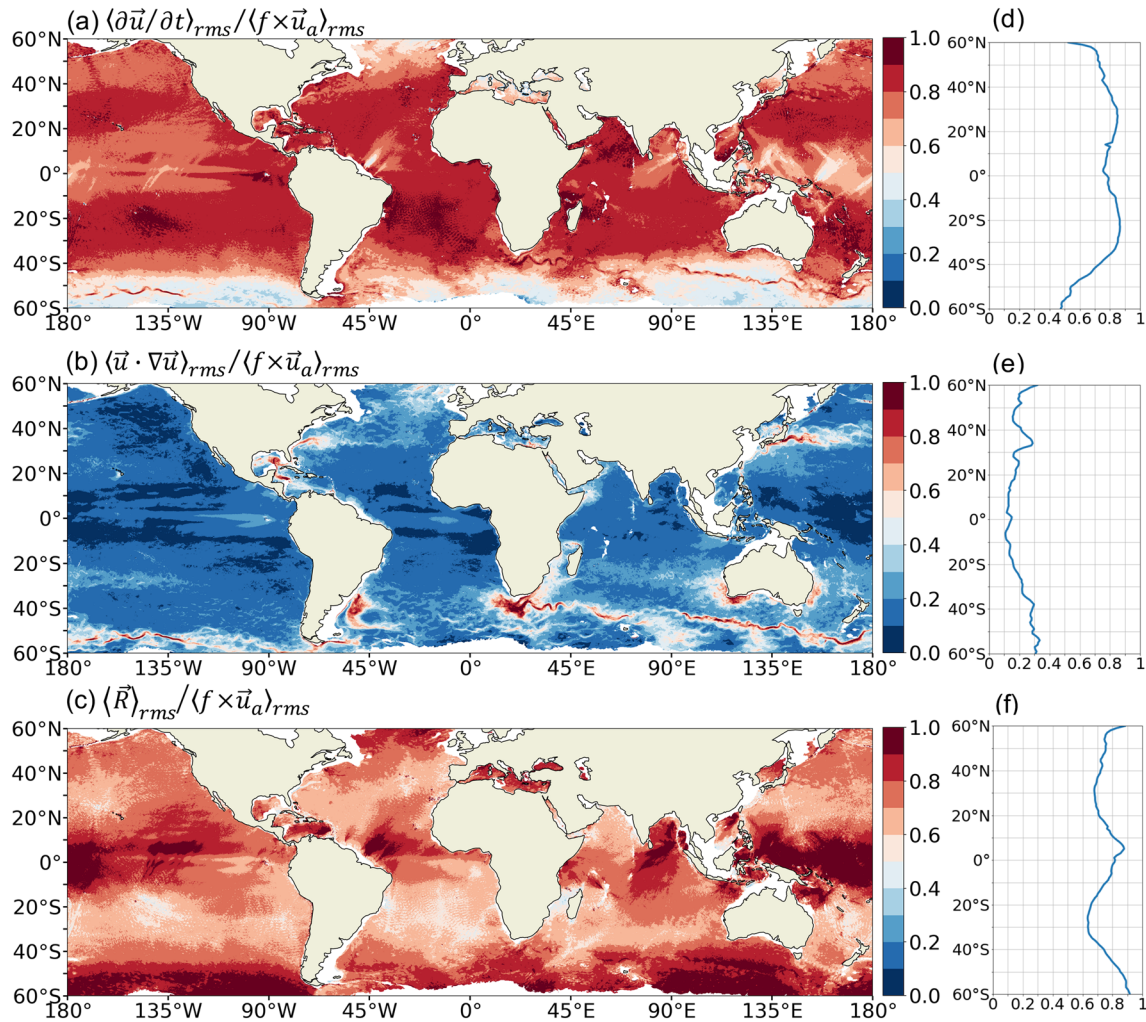


Figure 11. Fraction of each term to the ageostrophic Coriolis term. Global maps of the ratio of (a) the time acceleration term over the ageostrophic Coriolis term $\langle \partial \bar{u} / \partial t \rangle_{rms} / \langle f \times \bar{u}_a \rangle_{rms}$, (b) the advection term over the ageostrophic Coriolis term $\langle \bar{u} \cdot \nabla \bar{u} \rangle_{rms} / \langle f \times \bar{u}_a \rangle_{rms}$, and (c) the residual term over the ageostrophic Coriolis term $\langle \bar{R} \rangle_{rms} / \langle f \times \bar{u}_a \rangle_{rms}$. Their zonal averages are shown in (d–f).

atmospheric pressure fields. As a reminder, the inverted barometer effect predicts that a 1 mbar rise (fall) in air pressure causes a 1 cm fall (rise) in sea level elevation. The inverted barometer effect is partially satisfied in oceans (Carrere & Lyard, 2003). With altimetric observations of sea level, one benefits from operational estimates of the inverse barometer response and dynamic atmospheric corrections which would contribute to reduce the signature on sea level of the high-frequency barotropic response to atmospheric load and improve the comparison between surface currents and geostrophic ones.

The horizontal and vertical components of turbulent stress divergence was unfortunately not available from the LLC4320 output for this study, and are included in the momentum residual here. At the ocean surface, the turbulent stress divergence is typically dominated by the frictional stress driven by wind forcing, and may be approximated from wind stress. We estimate this vertical divergence of wind stress term using a scaling approximate of $\bar{F}_v \approx \frac{1}{\rho_0} \frac{\bar{\tau}}{\delta_e}$, where \bar{F}_v is the vertical component of the turbulent stress divergence, ρ_0

is the reference density, $\bar{\tau}$ is the surface wind stress, $\delta_e = \gamma u_* / f$ is the Ekman layer depth with $u_* = \sqrt{|\bar{\tau}| / \rho_0}$, and $\gamma = 0.25$ is an empirical constant determined from observations (Wang & Huang, 2004). The results indicate that the vertical divergence of wind stress term displays moderate large-scale structures at mid-latitudes and could explain much of the variance of the residual term there (not shown). In the tropical latitudes, however, the residual term is dominated by supertidal motions (Figure S3), and one could speculate

that the turbulent stress divergence associated with horizontal dissipation might also be responsible. Another limitation is that the LLC4320 simulation was stored as hourly snapshots, and thus the velocity and SSH fields alias variability higher than the model output frequency. To examine the impact of the turbulent stress divergence and higher-frequency (i.e., subhourly) variability, an online (i.e., during model run time) momentum budget analysis would be more adequate; a regional simulation in the tropical region forced by the LLC4320 boundary conditions will be considered in future work.

5. Summary

Geostrophy is a fundamental approximation that has been widely applied to the present altimetric SSH measurements on scales of a few hundreds of kilometers. In this study, we assess the global validity of geostrophy down to the spatial scale of $O(10\text{ km})$, using the hourly instantaneous surface fields from the tide- and eddy-resolving LLC4320 simulation. The degree of geostrophic validity at this scale is particularly relevant to the usage of 2D sea level measurements from the upcoming SWOT mission. Our main conclusions are summarized as follows:

1. Geostrophic balance is the leading-order balance and explains over 80% of variance in the regions of energetic kinetic energy, such as the western boundary currents and the ACC. In contrast, for the bulk of other open ocean regions, such as the eastern boundary currents and the interior of subtropical and subpolar gyres, surface currents geostrophically estimated from instantaneous sea level maps are significantly contaminated by fast variability and turbulent stress divergence, indicating geostrophy may not lead to accurate estimates of surface currents there if directly applied to SWOT instantaneous sea level maps. In the equatorial ocean, geostrophy does not hold due to the Coriolis parameter approaching zero.
2. The accuracy of geostrophy for the estimation of surface currents is frequency-dependent. Low-frequency component of the surface flows tends to follow the geostrophic balance to a first order almost across the global oceans away from the equator. The range of validity of geostrophy extends down to time scales of 20 days in the subtropical and subpolar oceans.
3. Contamination of geostrophically computed velocities by supertidal motions and localized internal tide motions dominates the resulting ageostrophic motions within tropical latitudes. The relative contribution of supertidal motions decreases toward higher latitudes such that internal tides and low-frequency contributions (associated with winds and advection) become dominant. Low-frequency Ekman flows are found to have an increasing contribution at higher latitudes.

Our findings point out that the limitation of geostrophy will prevent the direct estimation of surface currents from SWOT instantaneous sea level maps. This may be seen as a counterpart to the results of Qiu et al. (2018), who assessed the spatial scale dependency of separating balanced and unbalanced motions using the same model output. Both results indicate that balanced motions dominate unbalanced motions at large scales, and this tendency is highly dependent on local kinetic energy levels over the global oceans. In order to provide accurate surface current estimates, it will be necessary, away from energetic areas, either to identify and subtract high-frequency motions (including internal tides and internal wave continuum), or to low-pass filter SSH measurements temporally and/or spatially. In fact, spatial filtering may be the practical approach to mitigate the effects of fast variability given the long repeat sampling cycle (21 days) for SWOT, and to reduce instrumental noise (Chelton et al., 2019; Gómez-Navarro et al., 2018). Horizontal wavenumber spectra suggest that the effective horizontal resolution of LLC4320 is about 10 km (Rocha et al., 2016), which is finer than the scale that SWOT will resolve over the majority of the open ocean (15–50 km; Wang et al., 2019). One could expect the accuracy of geostrophy will increase at the SWOT resolution, due to the partial suppression of high-frequency unbalanced motions (e.g., some of the internal tides) at a coarser spatial scale. It is beyond the scope of the present study to assess the length scale dependency of geostrophy validity, a subject that would deserve dedicated efforts in the future.

Lastly, the numerical model study described here emphasized the importance of high-frequency motions in determining ageostrophic levels. In the real ocean, Lagrangian observations such as surface drifters provide a unique opportunity to better estimate high-frequency variability due to its high temporal resolution (approaching minutes with GPS tracking) and near-global spatial coverage (Elipot et al., 2016), although wave-vortex decomposition for Lagrangian data remains challenging (Wang & Bühler, 2021).

Data Availability Statement

The LLC output is available from the ECCO project (<https://data.nas.nasa.gov/ecco/data.php>).

Acknowledgments

This work was carried out as part of the ANR project number 17-CE01-0006-01 and entitled EQUINOX (Disentangling Quasi-geostrophic Motions and Internal Waves in High Resolution Satellite Observations of the Ocean). We thank the European Space Agency for funding the World Ocean Circulation (WOC) project in the frame of which this work was carried out. It is also part of the CNES-TOSCA project entitled “New Dynamical Tools for submesoscale characterization in SWOT data” that was proposed within the context of the SWOT mission. We thank three anonymous reviewers for insightful feedback.

References

- Arbic, B., Alford, M. H., Ansong, J. K., Buijsman, M. C., Ciotti, R. B., Farrar, J. T. (2018). A primer on global internal tide and internal gravity wave continuum modeling in HYCOM and MITgcm, et al. (Eds.), *New frontiers in operational oceanography* (pp. 307–392). GODAE OceanView.
- Ardhuin, F., Aksenov, Y., Benetazzo, A., Bertino, L., Brandt, P., Caubet, E., et al. (2018). Measuring currents, ice drift, and waves from space: The Sea surface Kinematics Multiscale monitoring (SKIM) concept. *Ocean Science*, *14*(3), 337–354. <https://doi.org/10.5194/os-14-337-2018>
- Ballarotta, M., Ubelmann, C., Pujol, M.-I., Taburet, G., Fournier, F., Legeais, J.-F., et al. (2019). On the resolutions of ocean altimetry maps. *Ocean Science*, *15*(4), 1091–1109. <https://doi.org/10.5194/os-15-1091-2019>
- Beardsley, R. C., Candela, J., Limeburner, R., Geyer, W. R., Lentz, S. J., Castro, B. M., et al. (1995). The M2 tide on the Amazon Shelf. *Journal of Geophysical Research: Oceans*, *100*, 2283. <https://doi.org/10.1029/94jc01688>
- Callies, J., Barkan, R., & Garabato, A. N. (2020). Time scales of submesoscale flow inferred from a mooring array. *Journal of Physical Oceanography*, *50*(4), 1065–1086. <https://doi.org/10.1175/jpo-d-19-0254.1>
- Callies, J., & Wu, W. (2019). Some expectations for submesoscale sea surface height variance spectra. *Journal of Physical Oceanography*, *49*(9), 2271–2289. <https://doi.org/10.1175/jpo-d-18-0272.1>
- Carrere, L., & Lyard, F. (2003). Modeling the barotropic response of the global ocean to atmospheric wind and pressure forcing—comparisons with observations. *Geophysical Research Letters*, *30*(6).
- Chelton, D. B., Schlax, M. G., & Samelson, R. M. (2011). Global observations of nonlinear mesoscale eddies. *Progress in Oceanography*, *91*(2), 167–216. <https://doi.org/10.1016/j.pocean.2011.01.002>
- Chelton, D. B., Schlax, M. G., Samelson, R. M., Farrar, J. T., Molemaker, M. J., McWilliams, J. C., & Gula, J. (2019). Prospects for future satellite estimation of small-scale variability of ocean surface velocity and vorticity. *Progress in Oceanography*, *173*, 256–350. <https://doi.org/10.1016/j.pocean.2018.10.012>
- Chen, G., Tang, J., Zhao, C., Wu, S., Yu, F., Ma, C., et al. (2019). Concept design of the “Guanlan” science mission: China’s novel contribution to space oceanography. *Frontiers in Marine Science*, *6*, 194. <https://doi.org/10.3389/fmars.2019.00194>
- Du, Y., Dong, X., Jiang, X., Zhang, Y., Zhu, D., Sun, Q., et al. (2021). Ocean surface current multiscale observation mission (OSCOM): Simultaneous measurement of ocean surface current, vector wind, and temperature. *Progress in Oceanography*, *193*, 102531. <https://doi.org/10.1016/j.pocean.2021.102531>
- Du Plessis, M., Swart, S., Anson, I. J., Mahadevan, A., & Thompson, A. F. (2019). Southern ocean seasonal restratification delayed by submesoscale wind–front interactions. *Journal of Physical Oceanography*, *49*(4), 1035–1053. <https://doi.org/10.1175/jpo-d-18-0136.1>
- Ekman, V. W. (1905). On the influence of the earth’s rotation on ocean currents. *Arkiv För Matematik, Astronomi Och Fysik*, *2*, 1–53.
- Eliot, S., Lumpkin, R., Perez, R. C., Lilly, J. M., Early, J. J., & Sykulski, A. M. (2016). A global surface drifter data set at hourly resolution. *Journal of Geophysical Research: Oceans*, *121*(5), 2937–2966. <https://doi.org/10.1002/2016jc011716>
- Eliot, S., Lumpkin, R., & Prieto, G. (2010). Modification of inertial oscillations by the mesoscale eddy field. *Journal of Geophysical Research: Oceans*, *115*. <https://doi.org/10.1029/2009jc005679>
- Emery, W. J., & Thomson, R. E. (2001). Chapter 5—Time-series analysis methods. In W. J. Emery & R. E. Thomson (Eds.), *Data analysis methods in physical oceanography* (pp. 371–567). Elsevier. <https://doi.org/10.1016/b978-044450756-3/50006-x>
- Ferrari, R., & Wunsch, C. (2009). Ocean circulation kinetic energy: Reservoirs, sources, and sinks. *Annual Review of Fluid Mechanics*, *41*, 253–282. <https://doi.org/10.1146/annurev.fluid.40.111406.102139>
- Flexas, M. M., Thompson, A. F., Torres, H. S., Klein, P., Farrar, J. T., Zhang, H., & Menemenlis, D. (2019). Global estimates of the energy transfer from the wind to the ocean, with emphasis on near-inertial oscillations. *Journal of Geophysical Research: Oceans*, *124*(8), 5723–5746. <https://doi.org/10.1029/2018jc014453>
- Forget, G., Campin, J. M., Heimbach, P., Hill, C. N., Ponte, R. M., & Wunsch, C. (2015). Ecco version 4: An integrated framework for non-linear inverse modeling and global ocean state estimation. *Geoscientific Model Development*, *8*(10), 3071–3104. <https://doi.org/10.5194/gmd-8-3071-2015>
- Fox-Kemper, B., & Menemenlis, D. (2008). Can large eddy simulation techniques improve mesoscale rich ocean models? In M. W. Hecht & H. Hasumi (Eds.), *Ocean modeling in an eddy regime* (pp. 319–337). American Geophysical Union. <https://doi.org/10.1029/177gm19>
- Fu, L.-L., & Pihos, G. (1994). Determining the response of sea level to atmospheric pressure forcing using topex/poseidon data. *Journal of Geophysical Research*, *99*(C12), 24633–24642.
- Gill, A. E. (1982). *Atmosphere-ocean dynamics*. Academic Press.
- Gómez-Navarro, L., Fablet, R., Mason, E., Pascual, A., Mourre, B., Cosme, E., & Le Sommer, J. (2018). SWOT spatial scales in the western Mediterranean Sea derived from pseudo-observations and an ad hoc filtering. *Remote Sensing*, *10*(4), 599. <https://doi.org/10.3390/rs10040599>
- Klein, P., Lapeyre, G., Siegelman, L., Qiu, B., Fu, L.-L., Torres, H., et al. (2019). Ocean-scale interactions from space. *Earth and Space Science*, *6*(5), 795–817. <https://doi.org/10.1029/2018ea000492>
- Lagerloef, G. S. E., Mitchum, G. T., Lukas, R. B., & Niiler, P. P. (1999). Tropical pacific near-surface currents estimated from altimeter, wind, and drifter data. *Journal of Geophysical Research: Oceans*, *104*(C10), 23313–23326. <https://doi.org/10.1029/1999jc900197>
- Lahaye, N., Gula, J., & Roulet, G. (2019). Sea surface signature of internal tides. *Geophysical Research Letters*, *46*(7), 3880–3890. <https://doi.org/10.1029/2018gl081848>
- Large, W. G., McWilliams, J. C., & Doney, S. C. (1994). Oceanic vertical mixing - A review and a model with a nonlocal boundary-layer parameterization. *Reviews of Geophysics*, *32*(4), 363–403. <https://doi.org/10.1029/94rg01872>
- Lévy, M., Franks, P. J. S., & Smith, K. S. (2018). The role of submesoscale currents in structuring marine ecosystems. *Nature Communications*, *9*, 4758. <https://doi.org/10.1038/s41467-018-07059-3>
- Luecke, C. A., Arbic, B. K., Richman, J. G., Shriver, J. F., Alford, M. H., Ansong, J. K., & Zamudio, L. (2020). Statistical comparisons of temperature variance and kinetic energy in global ocean models and observations: Results from mesoscale to internal wave frequencies. *Journal of Geophysical Research: Oceans*, *125*(5), e2019JC015306. <https://doi.org/10.1029/2019jc015306>

- Lumpkin, R., & Johnson, G. C. (2013). Global ocean surface velocities from drifters: Mean, variance, El Niño-Southern Oscillation response, and seasonal cycle. *Journal of Geophysical Research: Oceans*, 118(6), 2992–3006. <https://doi.org/10.1002/jgrc.20210>
- Marshall, J., Adcroft, A., Hill, C., Perelman, L., & Heisey, C. (1997). A finite-volume, incompressible Navier Stokes model for studies of the ocean on parallel computers. *Journal of Geophysical Research: Oceans*, 102(C3), 5753–5766. <https://doi.org/10.1029/96jc02775>
- McWilliams, J. C. (2016). Submesoscale currents in the ocean. *Proceedings of the Royal Society A: Mathematical, Physical and Engineering Sciences*, 472(2189). <https://doi.org/10.1098/rspa.2016.0117>
- Morrow, R., Fu, L. L., Arduin, F., Benkiran, M., Chapron, B., Cosme, E., et al. (2019). Global observations of fine-scale ocean surface topography with the surface water and ocean topography (SWOT) mission. *Frontiers in Marine Science*, 6, 232. <https://doi.org/10.3389/fmars.2019.00232>
- Morrow, R., & Le Traon, P. Y. (2012). Recent advances in observing mesoscale ocean dynamics with satellite altimetry. *Advances in Space Research*, 50(8), 1062–1076. <https://doi.org/10.1016/j.asr.2011.09.033>
- Müller, M., Arbic, B. K., Richman, J. G., Shriver, J. F., Kunze, E. L., Scott, R. B., et al. (2015). Toward an internal gravity wave spectrum in global ocean models. *Geophysical Research Letters*, 42(9), 3474–3481. <https://doi.org/10.1002/2015gl063365>
- Nelson, A. D., Arbic, B. K., Menemenlis, D., Peltier, W. R., Alford, M. H., Grisouard, N., & Klymak, J. M. (2020). Improved internal wave spectral continuum in a regional ocean model. *Journal of Geophysical Research: Oceans*, 125(5). <https://doi.org/10.1029/2019jc015974>
- Penven, P., Halo, I., Pous, S., & Marié, L. (2014). Cyclogeostrophic balance in the Mozambique Channel. *Journal of Geophysical Research: Oceans*, 119(2), 1054–1067. <https://doi.org/10.1002/2013jc009528>
- Ponte, A. L., Klein, P., Dunphy, M., & Le Gentil, S. (2017). Low-mode internal tides and balanced dynamics disentanglement in altimetric observations: Synergy with surface density observations. *Journal of Geophysical Research: Oceans*, 122(3), 2143–2155. <https://doi.org/10.1002/2016jc012214>
- Qiu, B., Chen, S., Klein, P., Wang, J., Torres, H., Fu, L.-L., & Menemenlis, D. (2018). Seasonality in transition scale from balanced to unbalanced motions in the world ocean. *Journal of Physical Oceanography*, 48(3), 591–605. <https://doi.org/10.1175/jpo-d-17-0169.1>
- Ray, R. D., & Zaron, E. D. (2016). M2 internal tides and their observed wavenumber spectra from satellite altimetry. *Journal of Physical Oceanography*, 46, 3–22. <https://doi.org/10.1175/jpo-d-15-0065.1>
- Rimac, A., von Storch, J. S., Eden, C., & Haak, H. (2013). The influence of high-resolution wind stress field on the power input to near-inertial motions in the ocean. *Geophysical Research Letters*, 40(18), 4882–4886. <https://doi.org/10.1002/grl.50929>
- Rio, M.-H. (2003). High-frequency response of wind-driven currents measured by drifting buoys and altimetry over the world ocean. *Journal of Geophysical Research: Oceans*, 108, 3283. <https://doi.org/10.1029/2002jc001655>
- Rocha, C. B., Chereskin, T. K., Gille, S. T., & Menemenlis, D. (2016). Mesoscale to submesoscale wavenumber spectra in Drake Passage. *Journal of Physical Oceanography*, 46(2), 601–620. <https://doi.org/10.1175/jpo-d-15-0087.1>
- Rodríguez, E., Wineteer, A., Perkovic-Martin, D., Gal, T., Stiles, B. W., Niamsuwan, N., & Monje, R. R. (2018). Estimating ocean vector winds and currents using a ka-band pencil-beam Doppler scatterometer. *Remote Sensing*, 10(4). <https://doi.org/10.3390/rs10040576>
- Savage, A. C., Arbic, B. K., Alford, M. H., Ansong, J. K., Farrar, J. T., Menemenlis, D., et al. (2017a). Spectral decomposition of internal gravity wave sea surface height in global models. *Journal of Geophysical Research: Oceans*, 122(10), 7803–7821. <https://doi.org/10.1002/2017jc013009>
- Savage, A. C., Arbic, B. K., Richman, J. G., Shriver, J. F., Alford, M. H., Buijsman, M. C., et al. (2017b). Frequency content of sea surface height variability from internal gravity waves to mesoscale eddies. *Journal of Geophysical Research: Oceans*, 122(3), 2519–2538. <https://doi.org/10.1002/2016jc012331>
- Schubert, R., Gula, J., Greatbatch, R. J., Baschek, B., & Biastoch, A. (2020). The submesoscale kinetic energy cascade: Mesoscale absorption of submesoscale mixed layer eddies and frontal downscale fluxes. *Journal of Physical Oceanography*, 50(9), 2573–2589. <https://doi.org/10.1175/jpo-d-19-0311.1>
- Shrira, V. I., & Almelah, R. B. (2020). Upper-ocean Ekman current dynamics: A new perspective. *Journal of Fluid Mechanics*, 887, A24. <https://doi.org/10.1017/jfm.2019.1059>
- Siegelman, L., Klein, P., Rivière, P., Thompson, A. F., Torres, H. S., Flexas, M., & Menemenlis, D. (2020). Enhanced upward heat transport at deep submesoscale ocean fronts. *Nature Geoscience*, 13(1), 50–55. <https://doi.org/10.1038/s41561-019-0489-1>
- Su, Z., Torres, H., Klein, P., Thompson, A. F., Siegelman, L., Wang, J., & Hill, C. (2020). High-frequency submesoscale motions enhance the upward vertical heat transport in the global ocean. *Journal of Geophysical Research: Oceans*, 125(9), e2020JC016544. <https://doi.org/10.1029/2020jc016544>
- Su, Z., Wang, J., Klein, P., Thompson, A. F., & Menemenlis, D. (2018). Ocean submesoscales as a key component of the global heat budget. *Nature Communications*, 9(1), 775. <https://doi.org/10.1038/s41467-018-02983-w>
- Thomas, L. N., Tandon, A., & Mahadevan, A. (2008). Submesoscale processes and dynamics. In M. W. Hecht & H. Hasumi (Eds.), *Ocean modeling in an eddying regime* (pp. 17–38). American Geophysical Union. <https://doi.org/10.1029/177gm04>
- Torres, H. S., Klein, P., Menemenlis, D., Qiu, B., Su, Z., Wang, J. B., et al. (2018). Partitioning ocean motions into balanced motions and internal gravity waves: A modeling study in anticipation of future space missions. *Journal of Geophysical Research: Oceans*, 123(11), 8084–8105. <https://doi.org/10.1029/2018jc014438>
- Vallis, G. (2006). *Atmospheric and oceanic fluid dynamics: Fundamentals and large-scale circulation* (p. 745). Cambridge University Press.
- Wang, H., & Bühler, O. (2021). Anisotropic statistics of Lagrangian structure functions and Helmholtz decomposition. *Journal of Physical Oceanography*, 51(5), 1375–1393. <https://doi.org/10.1175/jpo-d-20-0199.1>
- Wang, J., Fu, L. L., Torres, H. S., Chen, S. M., Qiu, B., & Menemenlis, D. (2019). On the spatial scales to be resolved by the surface water and ocean topography ka-band radar interferometer. *Journal of Atmospheric and Oceanic Technology*, 36(1), 87–99. <https://doi.org/10.1175/jtech-d-18-0119.1>
- Wang, W., & Huang, R. X. (2004). Wind energy input to the Ekman layer. *Journal of Physical Oceanography*, 34(5), 1267–1275. [https://doi.org/10.1175/1520-0485\(2004\)034<1267:weitte>2.0.co;2](https://doi.org/10.1175/1520-0485(2004)034<1267:weitte>2.0.co;2)
- Wunsch, C., & Stammer, D. (1997). Atmospheric loading and the oceanic “inverted barometer” effect. *Reviews of Geophysics*, 35(1), 79–107.
- Yu, X., Naveira Garabato, A. C., Martin, A. P., Buckingham, C. E., Brannigan, L., & Su, Z. (2019a). An annual cycle of submesoscale vertical flow and restratification in the upper ocean. *Journal of Physical Oceanography*, 49(6), 1439–1461. <https://doi.org/10.1175/jpo-d-18-0253.1>
- Yu, X., Naveira Garabato, A. C., Martin, A. P., & Marshall, D. P. (2021). The annual cycle of upper-ocean potential vorticity and its relationship to submesoscale instabilities. *Journal of Physical Oceanography*, 51(2), 385–402. <https://doi.org/10.1175/jpo-d-20-0099.1>

- Yu, X., Ponte, A. L., Elipot, S., Menemenlis, D., Zaron, E. D., & Abernathey, R. (2019b). Surface kinetic energy distributions in the global oceans from a high-resolution numerical model and surface drifter observations. *Geophysical Research Letters*, *46*(16), 9757–9766. <https://doi.org/10.1029/2019gl083074>
- Zhao, Z. (2014). Internal tide radiation from the Luzon Strait. *Journal of Geophysical Research: Oceans*, *119*, 5434–5448. <https://doi.org/10.1002/2014jc010014>